nature nanotechnology

LETTERS

https://doi.org/10.1038/s41565-019-0467-1

Defect induced, layer-modulated magnetism in ultrathin metallic $PtSe_2$

Ahmet Avsar[1,2*], Alberto Ciarrocchi[1,2], Michele Pizzochero[3], Dmitrii Unuchek[1,2], Oleg V. Yazyev[3] and Andras Kis[1,2*]

Defects are ubiquitous in solids and often introduce new properties that are absent in pristine materials. One of the opportunities offered by these crystal imperfections is an extrinsically induced long-range magnetic ordering[1], a long-time subject of theoretical investigations[1–3]. Intrinsic, two-dimensional (2D) magnetic materials[4–7] are attracting increasing attention for their unique properties, which include layer-dependent magnetism[4] and electric field modulation[6]. Yet, to induce magnetism into otherwise non-magnetic 2D materials remains a challenge. Here we investigate magneto-transport properties of ultrathin $PtSe_2$ crystals and demonstrate an unexpected magnetism. Our electrical measurements show the existence of either ferromagnetic or antiferromagnetic ground-state orderings that depends on the number of layers in this ultrathin material. The change in the device resistance on the application of a ~25 mT magnetic field is as high as 400 Ω with a magnetoresistance value of 5%. Our first-principles calculations suggest that surface magnetism induced by the presence of Pt vacancies and the Ruderman–Kittel–Kasuya–Yosida (RKKY) exchange couplings across ultrathin films of $PtSe_2$ are responsible for the observed layer-dependent magnetism. Given the existence of such unavoidable growth-related vacancies in 2D materials[8,9], these findings can expand the range of 2D ferromagnets into materials that would otherwise be overlooked.

Although intrinsically magnetic materials are rare in nature, long-range magnetism can be introduced into non-magnetic 2D materials through adatom intercalation[10], proximity coupling[11] and defect engineering[12] thanks to their large surface area to volume ratios. The latter strategy has been predicted for several 2D metallic materials, including graphene[2], but this has not been experimentally realized yet. Recently, $PtSe_2$ was considered to be an ideal platform to investigate defect-induced magnetization[13,14]. First-principles calculations show that Se and, especially, Pt vacancies in monolayer $PtSe_2$ have a strong influence on its electronic properties; a large magnetic moment of up to $6\mu_B$ is expected for single or double Pt vacancies. Such defects in 2D materials can either form naturally during the growth and annealing processes[8] or they can be intentionally created postsynthesis, for example, under electron-beam irradiation[15]. Point defects, which include Pt vacancies, are present at the topmost layers of $PtSe_2$ grown by chemical vapour transport[9]. Given the existence of these unavoidable point defects in as-grown material[9] and its metallic behaviour above a critical thickness[16,17], $PtSe_2$ holds a great promise for spintronic applications.

We obtained thin, ribbon-shaped $PtSe_2$ flakes by mechanical exfoliation from bulk crystals grown by chemical vapour transport (HQ Graphene) onto a Si/SiO_2 (270 nm) substrate. In total, ten devices were characterized with $PtSe_2$ thicknesses that varied between ~4.15 and ~14 nm, as determined by atomic force microscopy (AFM), which allowed us to study the thickness dependence of the magnetism. Non-magnetic metallic palladium (Pd) contacts (80 nm thick) were formed using electron-beam lithography and electron-beam evaporation techniques. These non-magnetic Pd contacts were fabricated to exclude any influence of the contact on the magnetic response of the device. Owing to the ribbon-like shape of our crystals, devices were fabricated in the two-terminal geometry. An AFM image of a completed device is shown in Fig. 1a. The longitudinal device resistance was characterized as a function of back-gate voltage (V_{BG}), source-drain bias (V_{SD}), magnetic field and temperature.

We first discuss the charge-transport properties of a device based on a 5.2 nm thick $PtSe_2$ crystal (device A). Figure 1b shows the gate-voltage (V_{BG}) dependence of the source-drain current (I_{SD}) at fixed bias-voltage (V_{SD}) values of 50, 100 and 200 mV at which we observe nearly gate-independent transport characteristics. This indicates that 5.2 nm $PtSe_2$ is metallic, in good agreement with recent findings[16,17]. This is also confirmed by the observation of a nearly linear I_{SD}–V_{SD} relation even at low temperatures (Fig. 1c) and by studying the temperature dependence of the device resistance (Supplementary Section 1). As semiconducting behaviour was observed in thinner samples (it is also challenging to electrically probe magnetism in such resistive samples (Supplementary Sections 2 and 3)), we focus on crystals thicker than 4.15 nm for the remainder of this article.

We utilized magnetoresistance measurements as a sensing tool to characterize the magnetism in $PtSe_2$. For this, we swept an out-of-plane magnetic field ($B_\perp$) while recording the device resistance. As shown in Fig. 2a, we observed a hysteresis loop with minima at ±25 mT under backward and forward scans. Such hysteretic behaviour and the presence of a minor loop (Supplementary Information 4) are the hallmarks of ferromagnetism and were previously observed in ferromagnetic metals such as cobalt (Co) under the same measurement geometry[18]. We extracted a coercive field of ~25 mT, which is comparable to that observed in Co wires[18]. We found a similar magnetoresistance response in four different samples with comparable coercive field values (Supplementary Section 5). We note that, just like the total device resistance, the change in the device resistance under a magnetic field was almost insensitive to the V_{BG} (Supplementary Section 6).

[1]Electrical Engineering Institute, École Polytechnique Fédérale de Lausanne (EPFL), Lausanne, Switzerland. [2]Institute of Materials Science and Engineering, École Polytechnique Fédérale de Lausanne (EPFL), Lausanne, Switzerland. [3]Institute of Physics, École Polytechnique Fédérale de Lausanne (EPFL), Lausanne, Switzerland. *e-mail: ahmet.avsar@epfl.ch; andras.kis@epfl.ch

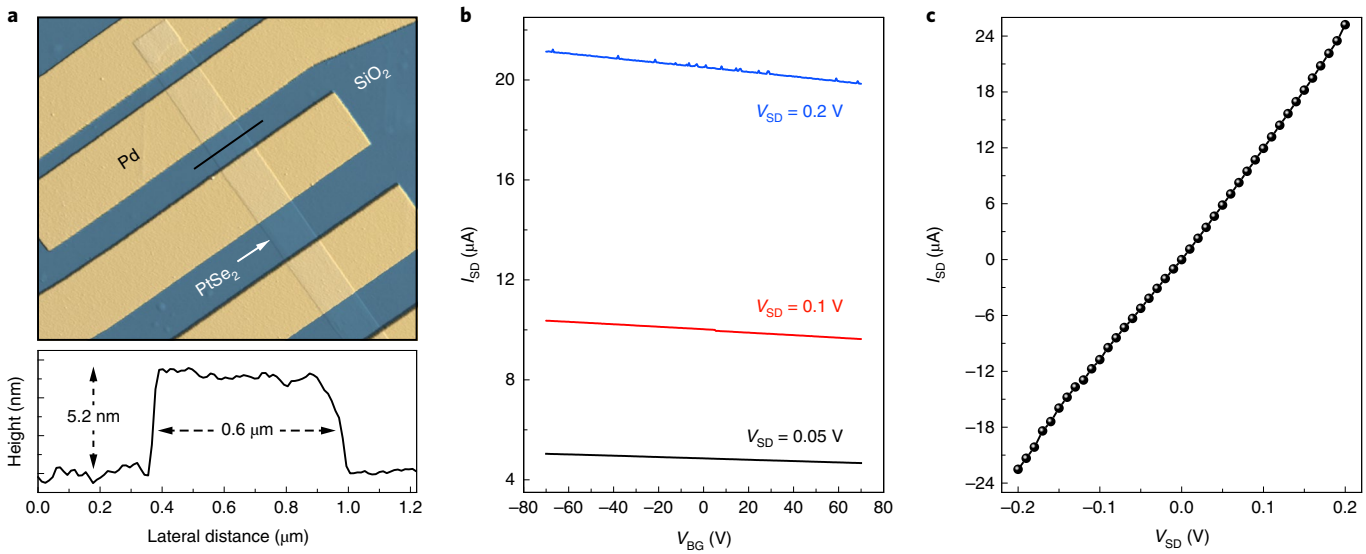

Fig. 1 | Device structure and basic characterization. a, An AFM image of device A. Height scale bar, ±40 nm. Following the black solid line, we measured a height of 5.2 nm and a width of 0.6 μm for this device. **b**, V_{BG} dependence of the I_{SD} measured at fixed V_{SD} values. **c**, Output characteristics of the device as a function of V_{SD} at a fixed V_{BG} of 0 V. All the charge-transport measurements were performed at 1.5 K.

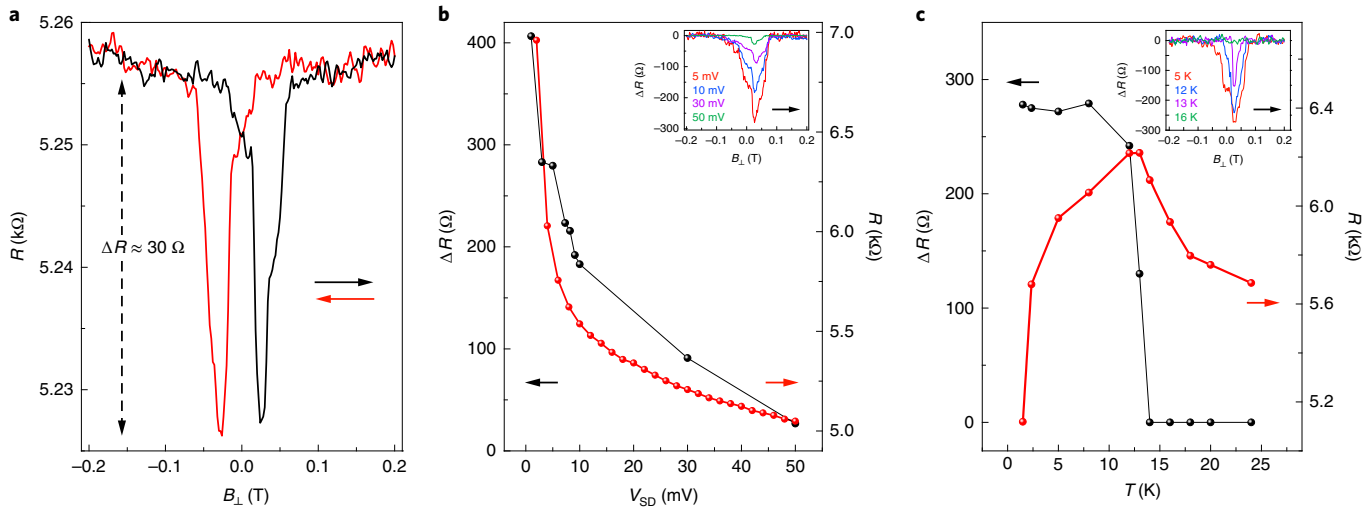

Fig. 2 | Bias and temperature-dependent magnetoresistance measurements in device A. a, Magnetic field dependence of the device resistance measured at $T = 1.6$ K with $V_{SD} = 50$ mV. The red (black) arrow represents the sweep direction from 0.2 T (−0.2 T) to −0.2 T (0.2 T). **b**, V_{SD} dependences of the change in the device resistance under a magnetic field (ΔR) and a longitudinal device resistance (R). The arrows indicate the relevant axes. Inset: resistance change under a magnetic field acquired at the fixed biases of $V_{SD} = 5$ mV, 10 mV, 30 mV and 50 mV. ΔR is calculated by subtracting a polynomial fitting from the device resistance (Supplementary Section 15). The arrow represents the direction of the magnetic field sweep. **c**, Temperature dependence of ΔR and R. The arrows indicate the relevant axes. Inset: magnetic field dependence of the resistance change measured at $T = 5$ K, 12 K, 13 K and 16 K. The arrow represents the direction of the magnetic field sweep.

Next, we studied the dependence of the change of device resistance (ΔR) on the bias voltage and the temperature. Figure 2b shows the V_{SD} dependence of ΔR measured at 1.6 K. The signal increases from $\Delta R = 30\,\Omega$ to $400\,\Omega$ as the bias is reduced from 50 mV to 1 mV. The extracted magnetoresistance percental variation is 5% at low biases (Supplementary Section 7). As shown in Fig. 2b, the dependencies of both ΔR and device resistance R on V_{SD} are similar and could be due to a slightly non-linear charge injection at low biases. Its physical origin needs further investigation. We also present the temperature dependence of the magnetoresistance measured at a fixed bias of $V_{SD} = 5$ mV (Fig. 2c). ΔR has a very weak temperature dependence in the $1.5\,\text{K} < T < 13\,\text{K}$ range. Raising the temperature just slightly over 13 K quickly suppresses the magnetic response of the device. The temperature dependence of the device resistance also shows a similar sudden drop when T is raised above 13 K, which could be related to the suppression of spin-dependent scattering. The resistance keeps increasing as the temperature is further increased, owing to the metallic nature of $PtSe_2$ (Supplementary Section 1).

In contrast to this hysteretic magneto-transport response, another subset that contained five out of ten characterized devices shows different characteristics (Supplementary Sections 8 and 9). In Fig. 3a, we show the magnetic field dependence (forward and backward sweep directions) of the device resistance for one of these devices

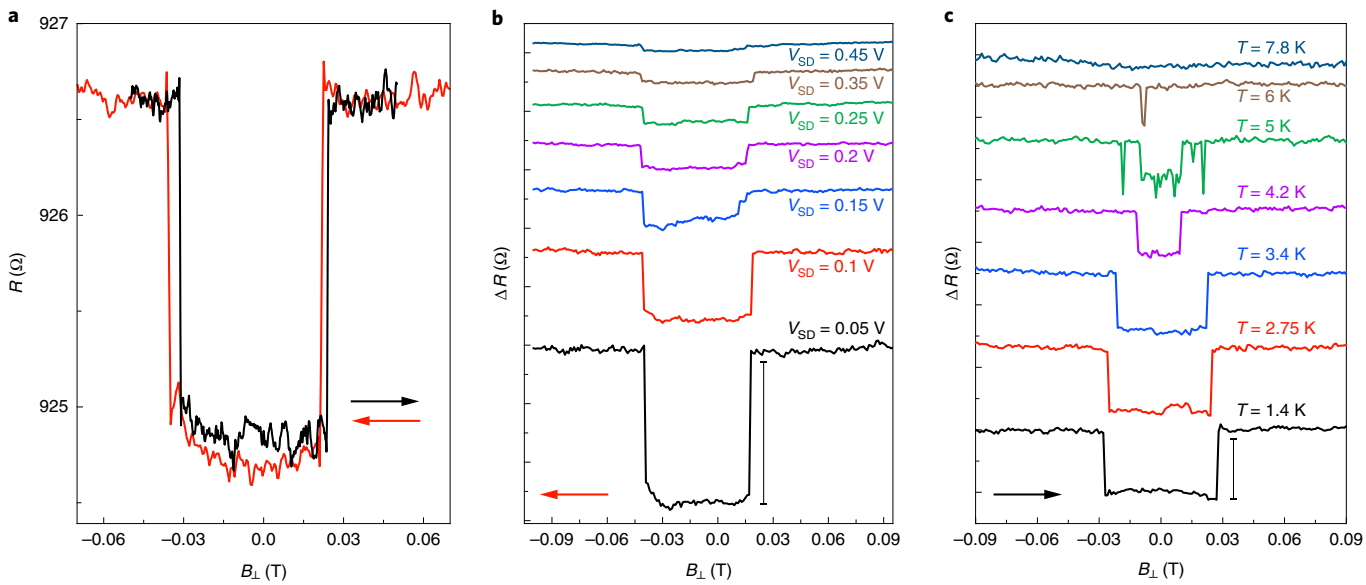

Fig. 3 | Bias and temperature-dependent magnetoresistance measurements in device B (~9 nm thick). a, Magnetic field dependence of the device resistance at $T = 1.6$ K and $V_{SD} = 100$ mV. **b**, V_{SD} dependence of the magnetoresistance change measured at $T = 1.6$ K. Scale bar, 5 Ω. The curves shown for the sweeps at $0.1\,V \leq V_{SD} \leq 0.45$ V are offset for clarity. **c**, Temperature dependence of ΔR measured at a fixed bias of $V_{SD} = 0.1$ V. Scale bar, 2 Ω. The curves shown for sweeps at $2.75\,K \leq T \leq 7.8$ K are offset for clarity. The red (black) arrows in all plots represent the sweep direction from positive (negative) to negative (positive) values.

(device B), which exhibits plateaus with two different values. Here we observe a lower plateau at low fields in the $-30\,mT < B < 30$ mT range, whereas a sharp jump to the high plateau is observed for fields above |30| mT. The height of the jump in this device is $\Delta R \approx 2\,\Omega$ and depends on the V_{SD}, as shown in Fig. 3b. The width and height of this plateau are also strongly sensitive to the temperature, as the signal completely disappears above 5 K (Fig. 3c). Here we are confident that the transition between these plateaus is a result of the switching between antiferromagnetic ordering at low fields into a fully spin-polarized state at higher fields due to the metamagnetic effect[19]. Such a magneto-transport response with two plateaus was previously observed in semiconducting bilayer CrI_3-based tunnelling devices[20,21]. It was shown that each CrI_3 layer initially has an opposite spin polarization at low fields and that the application of a field above the coercive field reverses the magnetization of one of CrI_3 layers to cause both layers to have the same spin polarization. Additionally, the observation of a very sharp switching between the low and high plateaus indicates the out-of-plane direction magneto-crystalline anisotropy of $PtSe_2$, in good agreement with recent predictions[14]. If the anisotropy had in-plane components, the switching would occur gradually with the field.

With the existence of both ferromagnetic and antiferromagnetic ordering in metallic $PtSe_2$ established, we next checked if there was a dependence of magnetization on the number of layers. The natural way to investigate this dependence would be to compare magneto-transport response of mono and bilayer $PtSe_2$. $PtSe_2$ is, however, extremely resistive in this thickness range[16]. Instead, we characterized two adjacent devices prepared under identical conditions. As confirmed by the AFM scan, the thickness of $PtSe_2$ crystals in these devices differs by only one layer, as shown in Fig. 4a,b, which allowed us to investigate layer-dependent magnetism. Although the device with 6.45 nm thick (10–11 layers, device C) $PtSe_2$ shows a characteristic response with two plateaus (Fig. 4c), the device with an extra layer (device D) shows a ferromagnetic response (Fig. 4d). This observation indicates the layer-dependent magnetism in $PtSe_2$. To investigate this effect further, we prepared another $PtSe_2$ device (device E) that contained additional one-layer thick fragments on the channel surface, as revealed by AFM imaging (Fig. 4e). The magneto-transport response of this sample is very intriguing: both ferromagnetic and antiferromagnetic ordering coexist (Fig. 4f). This measurement also allows us to conclude directly that the switching fields for these two contrasting magnetic orderings are different. Here the strong layer-dependent relationship between different mechanisms could be stabilizing the magnetic ordering differently and hence results in different switching fields. This observation is in good agreement with the different coercive fields probed by magneto-optic Kerr effect (MOKE) measurements for the even and odd layers of insulating CrI_3 magnets[4]. The existence of either ferromagnetic or antiferromagnetic ground-state orderings depending on the number of layers is intriguing.

In the following, we propose a theoretical picture to interpret the observed effects. As pristine $PtSe_2$ does not present any intrinsic spin polarization, either in bulk or in ultrathin multilayer form, we suggest that the observed magnetism originates from lattice imperfections (Supplementary Section 10). The appropriate model that describes the interaction between magnetic impurities mediated by conduction electrons is the well-established RKKY model[22–24]. According to this, the dependence of magnetic exchange coupling J on the distance R reads as $J(R) \approx \cos(2k_F R)/R^{\alpha}$, where k_F is the Fermi wavevector of the metal that hosts the magnetic impurities. The Fermi surface of $PtSe_2$ is composed of closed electron and hole pockets located at $k_z = 0$ and electron pockets at $k_z = \pm 0.6\pi/c$ (refs. [25,26]), where c is the lattice constant equal to the thickness of one layer and k_z is the momentum along its direction. The latter give rise to an oscillating and power-law decaying contribution to $J(R)$ in the direction normal to the $PtSe_2$ layers with a period of approximately two layers, as schematically shown in Fig. 5a. Hence, we see that to add or remove one layer from metallic $PtSe_2$ is sufficient to change the sign of the magnetic exchange coupling, and thereby realize a thickness-dependent ferro- or antiferromagnetic configuration. This observation is also in a good agreement with the summary of devices measured at fixed biases of $V_{SD} = 50$ mV and 100 mV. As shown in the Fig. 5a inset and Supplementary Section 12, we observe that magnetoresistance decreases as the crystal thickness

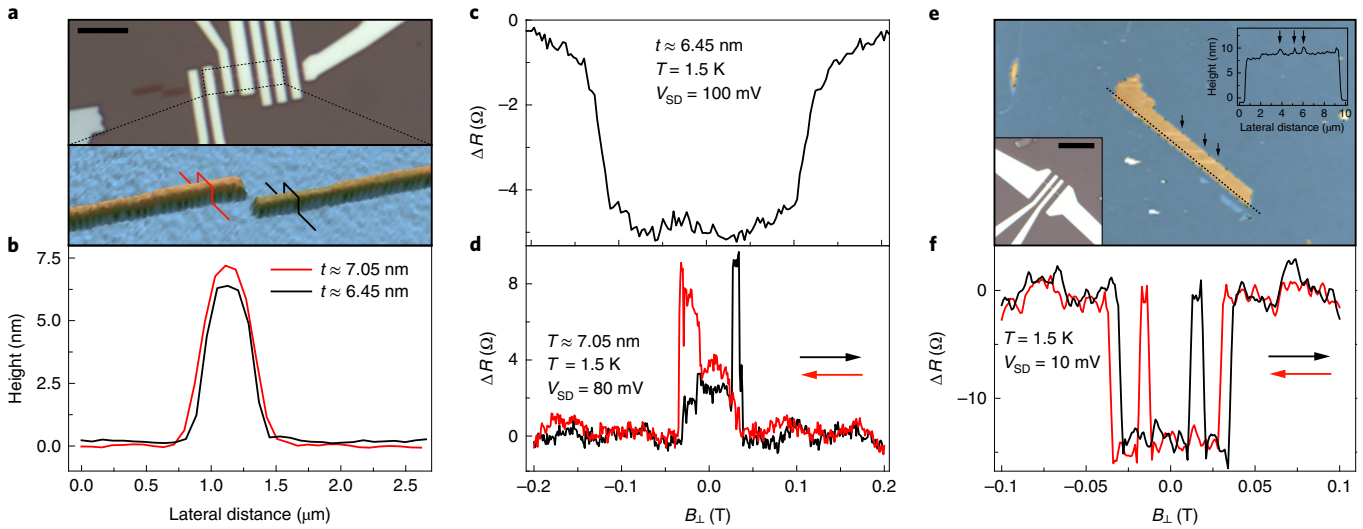

Fig. 4 | Layer-dependent magnetoresistance measurements. a, Optical (top) and AFM (bottom) images of a completed $PtSe_2$ device and its crystal, respectively. The dashed area represents the scanned AFM region. **b**. Cross-sectional plots along the red and black lines in **a**. AFM scans show that crystals used in devices C and D have a one-layer difference (~0.6 nm) in their heights. *t*, thickness. **c**, Magnetic field dependence of ΔR measured from device C (6.45 nm thick) at $T = 1.5$ K and $V_{SD} = 100$ mV. **d**, Magnetic field dependence of ΔR measured from device D (~7.05 nm thick) at $T = 1.5$ K and $V_{SD} = 80$ mV. The red (black) arrow represents the sweep direction from positive (negative) to negative (positive) values. **e**, AFM image of a $PtSe_2$ crystal with multiple one-layer thick fragments on its surface. Top inset: cross-sectional plots along the black dotted line in **e**. Black arrows in **e** and the top-inset of **e** indicate the one-layer thick fragments. Bottom inset: optical image of the corresponding device. Scale bar, 5 μm. **f**, Magnetic field dependence of ΔR measured from device E (shown in **e**) at $T = 1.5$ K and $V_{SD} = 10$ mV. The red (black) arrow represents the sweep direction from positive (negative) to negative (positive) values. We note that the change in device resistance in these samples has the opposite sign compared to the thinner devices shown in Fig. 2a and Supplementary Fig. 4a. Such opposite switching signs were previously observed in Co and CoFe films[35]. To determine the origin of this behaviour, the effect of the number of layers, distribution of defects and their effect on magnetism need to be extensively investigated.

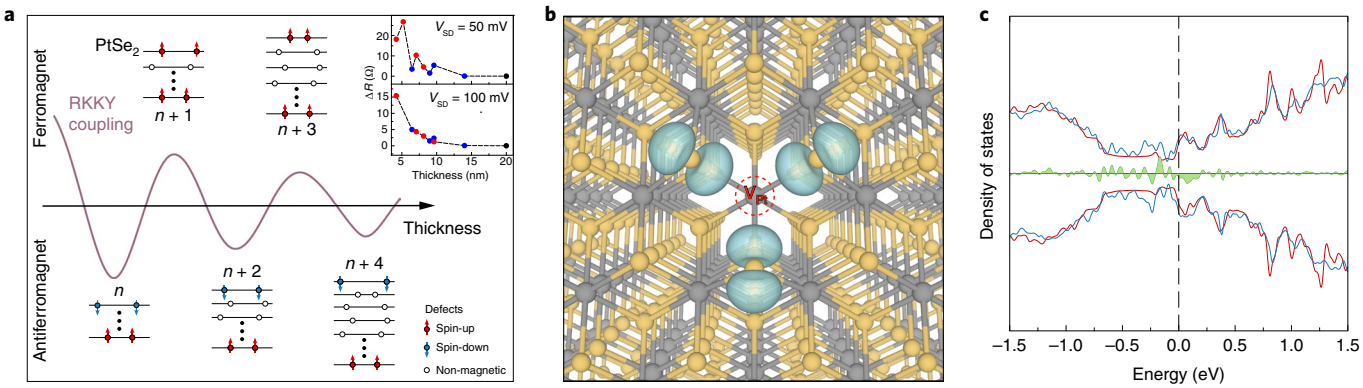

Fig. 5 | Theoretical investigations of $PtSe_2$. a, The schematic illustration shows the oscillating RKKY interaction across the $PtSe_2$ slab and the corresponding ground-state magnetic configurations. Inset: thickness dependence of the magnetoresistance curves for the studied samples at fixed V_{SD} of 50 mV (top) and 100 mV (bottom). Red circles, ferromagnetic; blue circles, antiferromagnetic; black circles, non-magnetic. *n* is the number of layers. **b**, Atomic structure and spin density (turquoise) around a surface V_{Pt} defect (red dotted circle) in multilayer $PtSe_2$. Grey (orange) balls represent Pt (Se) atoms. The isosurfaces contour is set to 0.003e Å^{-3}. **c**, Electronic density of states of multilayer $PtSe_2$ with (blue) and without (red) a surface V_{Pt} defect. The difference between the spin majority (top) and spin minority (bottom) states is shown in green. The Fermi level is set to zero (vertical dashed line).

increases, layer-dependent magnetism exists and magnetism is not detectable in thicker crystals.

Next, we step from model interactions to first-principles calculations performed on realistic models to suggest which type of defects may be responsible for the magnetic response observed in our samples. Earlier experimental investigations revealed the abundance of vacancy point defects in $PtSe_2$ films[9]. Motivated by this, we assessed the impact of such defects on the magnetic properties of $PtSe_2$ by introducing Se (V_{Se}) and Pt (V_{Pt}) vacancies in both the metallic multilayer and bulk $PtSe_2$ models. In analogy with other transition metal dichalcogenides[27], we found that the V_{Se} defect does not lead to magnetism (Supplementary Section 10). However, the introduction of the V_{Pt} defect at the surface of the multilayer model induces a local magnetic moment of ~1.2 μ_B per defect. We further observed that the spin density around the V_{Pt} defect mostly localizes on the neighbouring selenium atoms within its first coordination shell, as shown in Fig. 5b. Additionally, the investigation of the electronic density of states reported in Fig. 5c indicates that the local magnetic moments stem from defect-induced spin-split states that emerge around the Fermi level. Remarkably, we found that the same defect does not lead to a local magnetic moment when it forms in the bulk (Supplementary Sections 10 and 12). Similarly, extrinsic adsorbates do not induce magnetism (Supplementary Section 11). Note in this context that $PtSe_2$ is more prone to hosting metal atom vacancies

than conventional group VI dichalcogenides (for example, MoS_2) as a consequence of the substantially lower formation energy that this defect exhibits in the former material[9] as compared to the latter[27].

In contrast to recently discovered intrinsic ferromagnets[4–6], $PtSe_2$ has some key advantages for immediate research: it is stable in its pristine form (Supplementary Section 13) without the need for an encapsulation process[17], it can be easily grown with various scalable methods[28] and it is readily isolated from its as-prepared substrate, which makes it transferrable to any arbitrary substrate[28]. Compared to these intrinsic metallic ferromagnets, the currently observed critical temperature in $PtSe_2$ is small. This could be, in principle, improved by control of the vacancy concentration (to increase the concentration and total magnitude of the resulting magnetic moment), control of the crystal thickness (to control the sign of the coupling and the switching fields as discussed above) and the Fermi energy level (to modulate the density of states at the Fermi level) in future experiments.

Contrary to the assumption that defects in 2D materials are detrimental for the overall crystal quality, defect engineering could be a key approach to enriching their functionality by inducing magnetism in air-stable materials. In the case of $PtSe_2$, combining the defect-induced magnetism with unique thickness-dependent properties could have several applications for realizing spintronic devices using atomically thin materials[29–31]. Thin semiconducting $PtSe_2$ could be utilized as a magnetic substrate for proximity studies[32,33]. On the other hand, thick metallic $PtSe_2$ could be integrated into lateral and vertical spin torque devices[34], tunnelling magnetoresistance devices[35] and spin valve devices[36] to generate spin polarized charge carriers.

Online content

Any methods, additional references, Nature Research reporting summaries, source data, statements of code and data availability and associated accession codes are available at https://doi.org/10.1038/s41565-019-0467-1.

Received: 20 October 2018; Accepted: 2 May 2019;
Published online: 17 June 2019

References

1. Esquinazi, P., Hergert, W., Spemann, D., Setzer, A. & Ernst, A. Defect-induced magnetism in solids. *IEEE Trans. Magn.* **49**, 4668–4674 (2013).
2. Yazyev, O. V. & Helm, L. Defect-induced magnetism in graphene. *Phys. Rev. B* **75**, 125408 (2007).
3. Osorio-Guillén, J., Lany, S., Barabash, S. V. & Zunger, A. Magnetism without magnetic ions: percolation, exchange, and formation energies of magnetism-promoting intrinsic defects in CaO. *Phys. Rev. Lett.* **96**, 107203 (2006).
4. Huang, B. et al. Layer-dependent ferromagnetism in a van der Waals crystal down to the monolayer limit. *Nature* **546**, 270–273 (2017).
5. Gong, C. et al. Discovery of intrinsic ferromagnetism in two-dimensional van der Waals crystals. *Nature* **546**, 265–269 (2017).
6. Deng, Y. et al. Gate-tunable room-temperature ferromagnetism in two-dimensional Fe_3GeTe_2. *Nature* **563**, 94–99 (2018).
7. Bonilla, M. et al. Strong room-temperature ferromagnetism in VSe_2 monolayers on van der Waals substrates. *Nat. Nanotechnol.* **13**, 289–293 (2018).
8. Zhou, W. et al. Intrinsic structural defects in monolayer molybdenum disulfide. *Nano Lett.* **13**, 2615–2622 (2013).
9. Zheng, H. et al. Intrinsic point defects in ultrathin 1T-$PtSe_2$ layers. Preprint at https://arxiv.org/abs/1808.04719 (2018).
10. Hardy, W. J. et al. Very large magnetoresistance in $Fe_{0.28}TaS_2$ single crystals. *Phys. Rev. B* **91**, 054426 (2015).
11. Wang, Z., Tang, C., Sachs, R., Barlas, Y. & Shi, J. Proximity-induced ferromagnetism in graphene revealed by the anomalous Hall effect. *Phys. Rev. Lett.* **114**, 016603 (2015).
12. Guguchia, Z. et al. Magnetism in semiconducting molybdenum dichalcogenides. *Sci. Adv.* **4**, eaat3672 (2018).
13. Gao, J. et al. Structure, stability, and kinetics of vacancy defects in monolayer $PtSe_2$: a first-principles study. *ACS Omega* **2**, 8640–8648 (2017).
14. Zhang, W. et al. Magnetism and magnetocrystalline anisotropy in single-layer $PtSe_2$: interplay between strain and vacancy. *J. Appl. Phys.* **120**, 013904 (2016).
15. Krasheninnikov, A. V. & Nordlund, K. Ion and electron irradiation-induced effects in nanostructured materials. *J. Appl. Phys.* **107**, 071301 (2010).
16. Ciarrocchi, A., Avsar, A., Ovchinnikov, D. & Kis, A. Thickness-modulated metal-to-semiconductor transformation in a transition metal dichalcogenide. *Nat. Commun.* **9**, 919 (2018).
17. Zhao, Y. et al. High-electron-mobility and air-stable 2D layered $PtSe_2$ FETs. *Adv. Mater.* **29**, 1604230 (2017).
18. Leven, B. & Dumpich, G. Resistance behavior and magnetization reversal analysis of individual Co nanowires. *Phys. Rev. B* **71**, 064411 (2005).
19. Huang, F., Kief, M. T., Mankey, G. J. & Willis, R. F. Magnetism in the few-monolayers limit: a surface magneto-optic Kerr-effect study of the magnetic behavior of ultrathin films of Co, Ni, and Co–Ni alloys on Cu(100) and Cu(111). *Phys. Rev. B* **49**, 3962–3971 (1994).
20. Song, T. et al. Giant tunneling magnetoresistance in spin-filter van der Waals heterostructures. *Science* **360**, 1214–1218 (2018).
21. Klein, D. R. et al. Probing magnetism in 2D van der Waals crystalline insulators via electron tunneling. *Science* **360**, 1218–1222 (2018).
22. Ruderman, M. A. & Kittel, C. Indirect exchange coupling of nuclear magnetic moments by conduction electrons. *Phys. Rev.* **96**, 99–102 (1954).
23. Kasuya, T. A theory of metallic ferro- and antiferromagnetism on Zener's model. *Prog. Theor. Phys.* **16**, 45–57 (1956).
24. Yosida, K. Magnetic properties of Cu–Mn alloys. *Phys. Rev.* **106**, 893–898 (1957).
25. Zhang, K. et al. Experimental evidence for type-II Dirac semimetal in $PtSe_2$. *Phys. Rev. B* **96**, 125102 (2017).
26. Clark, O. J. et al. Dual quantum confinement and anisotropic spin splitting in the multivalley semimetal $PtSe_2$. *Phys. Rev. B* **99**, 045438 (2019).
27. Pizzochero, M. & Yazyev, O. V. Point defects in the 1T′ and 2H phases of single-layer MoS_2: a comparative first-principles study. *Phys. Rev. B* **96**, 245402 (2017).
28. Yu, X. et al. Atomically thin noble metal dichalcogenide: a broadband mid-infrared semiconductor. *Nat. Commun.* **9**, 1545 (2018).
29. Žutić, I., Fabian, J. & Das Sarma, S. Spintronics: fundamentals and applications. *Rev. Mod. Phys.* **76**, 323–410 (2004).
30. Han, W., Kawakami, R. K., Gmitra, M. & Fabian, J. Graphene spintronics. *Nat. Nanotechnol.* **9**, 794–807 (2014).
31. Wen, H. et al. Experimental demonstration of XOR operation in graphene magnetologic gates at room temperature. *Phys. Rev. Appl.* **5**, 044003 (2016).
32. Žutić, I., Matos-Abiague, A., Scharf, B., Dery, H. & Belashchenko, K. Proximitized materials. *Mater. Today* **22**, 85–107 (2019).
33. Scharf, B., Xu, G., Matos-Abiague, A. & Žutić, I. Magnetic proximity effects in transition-metal dichalcogenides: converting excitons. *Phys. Rev. Lett.* **119**, 127403 (2017).
34. Yang, T., Kimura, T. & Otani, Y. Giant spin-accumulation signal and pure spin–current-induced reversible magnetization switching. *Nat. Phys.* **4**, 851–854 (2008).
35. Moodera, J. S., Kinder, L. R., Wong, T. M. & Meservey, R. Large magnetoresistance at room temperature in ferromagnetic thin film tunnel junctions. *Phys. Rev. Lett.* **74**, 3273–3276 (1995).
36. Avsar, A. et al. Gate-tunable black phosphorus spin valve with nanosecond spin lifetimes. *Nat. Phys.* **13**, 888–893 (2017).

Acknowledgements

We acknowledge A. H. C. Neto for fruitful insights and discussions. We acknowledge the help of Z. Benes (CMI) with electron-beam lithography and K. Marinov for training on the measurement set-up. A.A., A.C., D.U. and A.K. acknowledge support by the European Research Council (ERC, grant 682332), Swiss National Science Foundation (grant 153298) and Marie Curie-Sklodowska COFUND (grant 665667). A.K. acknowledges funding from the European Union's Horizon 2020 research and innovation programme under grant agreement no 785219 (Graphene Flagship). M.P. and O.V.Y. acknowledge support by the Swiss National Science Foundation (grants 162612 and 172543). First-principles simulations were carried out at the Swiss National Supercomputing Centre (CSCS) under project s832.

Author contributions

A.A. and A.K. designed the experiments. A.A. and A.C. fabricated the samples. A.A. performed the transport measurements. A.C. and D.U. performed the Raman spectroscopy measurements. M.P. and O.V.Y. devised the theoretical models and performed the first-principles calculations. A.A., M.P. and A.K. wrote the manuscript with input from A.C.

Competing interests

The authors declare no competing interests.

Additional information

Supplementary information is available for this paper at https://doi.org/10.1038/s41565-019-0467-1.

Reprints and permissions information is available at www.nature.com/reprints.

Correspondence and requests for materials should be addressed to A.A. or A.K.

Publisher's note: Springer Nature remains neutral with regard to jurisdictional claims in published maps and institutional affiliations.

Methods

Device fabrication. $PtSe_2$ crystals were obtained by mechanical exfoliation from bulk crystals (HQ Graphene) onto a doped Si substrate with 270 nm of SiO_2. The substrate was imaged using a colour camera equipped optical microscope (Olympus BX51M). The thickness of the selected crystals was determined by using AFM topography imaging (Asylum Research Cypher). Metallic contacts were prepared using an electron-beam lithography (Raith EBPG 5000+, 100 keV thermal field emission gun with a beam dose of ~950 μC cm^{-2}) and electron-beam evaporation of Pd (Alliance-Concept EVA 760, 80 nm thick), without the use of any adhesion layers such as Cr or Ti.

Measurements. Cryogenic measurements were performed in an ICE Oxford liquid helium bath cryomagnetic system with a base temperature of ~1.5 K. Drain currents were measured using a Keithley Sourcemeter 2450, and a Keithley Sourcemeter 2400 was used to apply bias through the SiO_2 gate dielectric. The drain voltage was varied between 1 mV and 1 V with the source grounded. Electronic transport measurements were carried out in a two-terminal configuration.

First-principles calculations. First-principles calculations were performed within the generalized gradient approximation to density functional theory devised by Perdew et al.[37]. Geometry optimizations were carried out with the VASP code[38,39] using a kinetic energy cutoff of 400 eV and k meshes equivalent to 18 k points per unit cell along each periodic direction. During the geometry optimizations, the lattice constants and interlayer spacings were constrained to their experimental values of 3.73 Å and 5.08 Å, respectively, and the tolerance on atomic forces was set to 0.02 eV Å^{-1}. The electronic density of states was calculated with the SIESTA code[40], using a fine mesh equivalent to 120 k points and a smearing of 0.02 eV. The adopted multilayer and bulk $PtSe_2$ models consist of a six-layer thick 3 × 3 supercell and a periodic 3 × 3 × 2 supercell, respectively. In the case of the multilayer models, the defects were placed in the topmost layer and a vacuum region of 15 Å was introduced to separate the periodic images.

Data availability

The data that support the findings of this study are available from the corresponding authors on reasonable request.

References

37. Perdew, J. P., Burke, K. & Ernzerhof, M. Generalized gradient approximation made simple. *Phys. Rev. Lett.* **77**, 3865–3868 (1996).
38. Kresse, G. & Furthmüller, J. Efficient iterative schemes for ab initio total-energy calculations using a plane-wave basis set. *Phys. Rev. B* **54**, 11169–11186 (1996).
39. Kresse, G. & Joubert, D. From ultrasoft pseudopotentials to the projector augmented-wave method. *Phys. Rev. B* **59**, 1758–1775 (1999).
40. Soler, J. M. et al. The SIESTA method for ab initio order-N materials simulation. *J. Phys. Condens. Matter* **14**, 2745 (2002).